A Spine-Specific Phased Array for Transvertebral Ultrasound Therapy: Design & Simulation

Rui Xu, Meaghan A. O'Reilly, *Member, IEEE*

Abstract*—*Objective: **To design and simulate the performance of two spine-specific phased arrays in sonicating targets spanning the thoracic spine, with the objective of efficiently producing controlled foci in the spinal canal.** ***Methods:*** **Two arrays (256 elements each, 500 kHz) were designed using multi-layered ray acoustics simulation; a 4-component array with dedicated components for sonicating via the paravertebral and transvertebral paths, and a 2-component array with spine-specific adaptive focusing. Mean array efficiency (canal focus pressure/water focus pressure) was evaluated using forward simulation in neutral and flexed spines to investigate methods that reduce spine-induced insertion loss. Target-specific 4-component array reconfiguration and lower frequency sonication (250 kHz) were tested to determine their effects on array efficiency and focal dimensions.** ***Results:*** **When neutral, 2- and 4-component efficiencies were $32 \pm 11\%$ and $29 \pm 13\%$ respectively. Spine flexion significantly increased 4-component efficiency ($36 \pm 18\%$), but not 2-component efficiency ($33 \pm 15\%$). Target-specific 4-component re-configuration significantly improved efficiency ($36 \pm 8\%$). Both arrays produced controlled foci centered within the canal with similar 50% pressure contour dimensions: 10.8-11.9 mm (axial), 4.2-5.6 mm (lateral), and 5.9-6.2 mm (vertical). Simulation at 250 kHz also improved 2- and 4-component efficiency ($43 \pm 17\%$ and $36 \pm 13\%$ respectively), but doubled the lateral focal dimensions.** ***Conclusion:*** **Simulation shows that the spine-specific arrays are capable of producing controlled foci in the thoracic spinal canal.** ***Significance:*** **The complex geometry of the human spine presents geometrical and acoustical challenges for transspine ultrasound focusing, and the design of these spine-specific ultrasound arrays is crucial to the clinical translation of focused ultrasound for the treatment of spinal cord disease.**

***Index Terms*—Focused Ultrasound, Spine, Phased Array.**

I. Introduction

FOCUSED ultrasound is poised to transform brain therapy via non-invasive functional neurosurgery [1], [2], targeted drug delivery [3], and neuromodulation [4]. Similar opportunities exist for the spinal cord. For example, pre-clinical studies have demonstrated that ultrasound can safely increase blood-spinal cord barrier permeability in small animals, improving targeted therapeutic delivery to the spinal cord [5]–[7]. A key challenge to the clinical translation of focused ultrasound spinal cord therapy is the difficulty in focusing ultrasound through the human spine to the vertebral canal. Bone has acoustic properties that differ drastically from soft tissues [8]–[10]. Combined with the complex geometry of human vertebrae, these acoustic mismatches result in wavefront distortion and focal aberrations that are highly dependent on the vertical level of the spinal cord target [11].

Safe and accurate transspinal focused ultrasound requires beamforming to compensate for vertebra-induced ultrasound wavefront aberration. A phased array is necessary for transspinal-ultrasound applications, given the requisite variability in beamforming necessary for treating the irregularity of the spine. Phased arrays have been designed for many therapeutic applications, including hemispherical and/or patient specific arrays that focus ultrasound through the skull [12]–[17] using aberration correction [13], [18] based on prior x-ray computed tomography (CT)-based acoustic properties [10], [19], [20], and a commercial device exists (ExAblate Neuro, InSightec). While the geometry of the skull guides the design of conformal and hemispherical transkull arrays, the geometry of the spine gives less intuition to the design of a spine-specific phased array.

Several limitations for focusing ultrasound to the spinal cord must be addressed: the presence of ribs and lungs in the thorax constrains ultrasound delivery paths to a dorsal approach, and the distance from spinal cord to dorsal skin surface is 6-10 cm in the thoracic region in the Visible Human Project [21], and potentially more for large patients. These obstacles constrain potential array element positions. Two viable transspinal ultrasound propagation paths exist in the thorax: a paravertebral path, through the spaces between laminae, and a translaminar path, through the vertebral bone itself.

A transspine ray traced between a posterior source and target within the spinal cord may cross one bone layer, (e.g. along the translaminar path), two bone layers (e.g. along a medial path through overlapping of the spinous process with the posterior arch of the inferior vertebrae), or zero bone interfaces (e.g. through the paralaminar path). These transspine paths are shown in Fig. 1. The paralaminar path presents an opportunity to focus ultrasound directly to the spinal cord without the need to focus ultrasound through bone. The impedance mismatch between soft tissue and bone results in reflection from the interface, decreasing the efficacy of paths that intersect bone. For example, reflective pressure loss at normal incidence at one bone interface is approximately 30%, two bone layers, approximately 50%, with further losses at non-normal incidence [22], [23]. Given the irregularity of the spine and the highly attenuative nature of bone [10], [24], maximizing ultrasound propagation along paths that minimize bone intersection should minimize spine-induced insertion loss, maximizing array efficiency. Beamforming algorithms and phased arrays have been developed for transcostal applications, where there is a similar challenge of focusing ultrasound

Manuscript received February 1, 2019. This work was supported by the Natural Sciences and Engineering Council of Canada and the Ontario Ministry of Research, Innovation and Science Early Researcher Award Program.

R. Xu and M. A. O'Reilly are with the Physical Sciences Platform, Sunnybrook Research Institute, Toronto, ON, Canada and the Department of Medical Biophysics, University of Toronto, ON, Canada (rxu@sri.utoronto.ca)

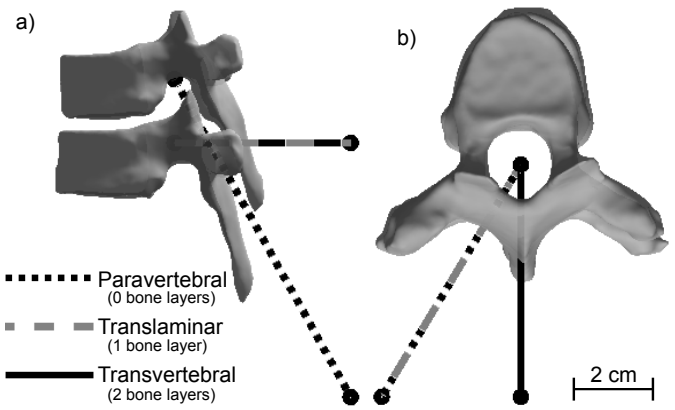

Fig. 1. a) Lateral and b) superior views of three paths (paravertebral, translaminar, transvertebral) from a posterior source to the vertebral canal.

through intercostal spaces [25]–[31]. However, the paralaminar space is smaller than the intercostal space [32], and some spinal cord targets will be geometrically occluded by the vertebral column. The thoracic region of the human spine is semi-deformable, with three degrees of freedom (flexion-extension, 28°; lateral bending, 36°; axial rotation, 45°) [33]. Sagittal spine flexion may increase the paravertebral space, increasing the number of targets accessible via the the paravertebral path. The translaminar path may be suitable for delivering ultrasound to targets that remain geometrically occluded, and has been investigated $ex\ vivo$ and $in\ silico$ using a single-element spherically focused transducer, with insertion losses on the order of 70% at 514 kHz [11], [34]. A spine-specific array capable of focusing ultrasound to targets spanning the height of the thoracic region of the spine must have the capacity to efficiently focus ultrasound through both paralaminar and translaminar paths. Efficient transspine focusing is essential for clinical translation of focused ultrasound spinal cord therapy. For example, McDannold et al., previously reported a threshold mechanical index (MI) of 0.46 for blood-brain barrier opening [35] using 20 second sonications, equivalent to approximately 0.33 MPa peak negative pressure at 500 kHz. However this value should be considered a rough guideline as longer sonications will decrease the pressure required to cause opening. In rat spinal cord, O'Reilly et al. reported a non-derated peak pressure 0.43 ± 0.09 MPa (approximately 0.29 MPa $in\ situ$) for 2 minute treatments using an active control method that modulates the treatment exposure based on the detect of sub or ultraharmonic signals [7].

In this study, we designed two spine-specific phased arrays using multi-layered ray acoustics simulation: a 4-component array with two dedicated components for translaminar propagation and two dedicated components for paravertebral propagation; and a 2-component array where each element propagation path is determined using an occlusion test, giving the array additional flexibility for treating variant paravertebral spaces. The motivation for designing the two arrays is to test the difference between an array where the elements have pre-determined propagation paths, and an array where the elements' propagation path is determined on a target-by-target basis. We test two additional hypotheses, both motivated by the geometry of the spine: sagittal spine flexion, and target-specific array re-configuration to maximize path-specific transspine transmission will minimize spine-induced insertion loss and improve array efficiency. We report transspinal propagation efficiency and focal dimensions for targets spanning the height of the thoracic region of the spine for both arrays and both additional hypotheses, and discuss the merits of each approach.

II. Methods

A. Ultrasonic Approach

The geometry of the spine and rib cage point to an array placed posterior to the spine and capable of electronically focusing ultrasound through both paralaminar and translaminar paths. We measured four median and four paramedian (30° to median plane) distances from the canal center to dorsal skin surfaces per thoracic vertebra in the Visible Human Project (VHP) [21]. The mean median length was 63 ± 10 mm (range: 50 mm - 85 mm), and the mean paramedian length was 75 ± 14 mm (range: 57 mm - 103 mm). Comparison at the T5-T6 level to [36] showed that VHP distances were approximately 20 mm longer; a difference that may be ascribed to a higher body mass index in the VHP than the 40-individual sample in [36]. Following these measurements, we constrained array element positions to lie within a semi-cylindrical surface placed 12 cm posterior to the canal, allowing for a minimum 2 cm stand-off from the posterior skin surface. It is noted that the proposed designs may not be suitable for very large individuals. Further specification of the ultrasonic approach requires determining element shape, frequency, the number of elements, then determining optimal element positioning. These array parameters may be determined via numerical optimization, or informed via prior studies. Here, we based our choice of element frequency and shape on prior work [11], [16], the total number of array elements (256) on compatibility with commercially available beamforming hardware, then calculated optimal element positions using transvertebral ultrasound simulation. The transmission frequency used in [11], [34] of 514 kHz balanced the trade-off between small focal size and higher wavefront attenuation at high frequency vs. large focal size and lower wavefront attenuation a low frequency. Following from this work, we used a frequency of 500 kHz, and obtained array element dimensions by scaling the cylindrical element dimensions in [16], [37] to 500 kHz, resulting in 7.5 mm diameter cylindrical elements. 256 sparsely arranged elements of similar dimensions have been used for blood brain barrier opening [16], [37], and based on the maximum peak negative pressures reported for those devices, we expect our device will be able to generate sufficient *in situ* pressures for blood-spinal cord barrier opening. We also performed transvertebral ultrasound simulation with 250 kHz, as this lower frequency is less susceptible to aberration and attenuation, at the expense of a larger focal size.

B. in silico Design

We designed two spine-specific phased arrays using acoustic simulation, with the objective of maximizing ultrasound

transmission to the spinal cord at any vertical level within the thorax. The acoustic simulation is based on a multi-layered ray acoustics model of transvertebral ultrasound propagation [11]. Ray acoustics is an approximate numerical model based on the Rayleigh-Sommerfeld integral and accounts for the physics of acoustic waves incident on fluid-solid and solid-fluid interfaces, while remaining less computationally expensive than full-wave acoustic models [22], [38]–[40]. The low computational cost of the ray acoustics model is essential to performing the large set of simulations to test targets spanning the entire thoracic region of the spine.

1) Spine Simulation System: The simulation system is based on a re-hydrated $ex\ vivo$ adult human thoracic spine (Osta International, White Rock, BC, Canada). Vertebral body volume was measured and compared to [41], with an average vertebral body volume $5.4\% \pm 4.0\%$ smaller than the average male and $7.2\% \pm 5.6\%$ larger than the average female. We used the entire thoracic spine to account for differences in vertebral size and geometry between patients, as the intra-thoracic variation in vertebral size and geometry is generally larger than inter-vertebral variation at identical levels between different patients [41], [42]. All vertebrae were immersed in deionized water and degassed in a vacuum chamber (Nalgene vacuum chamber, Fisher Scientific; Gast, Benton Harbor, MI, USA) for several days, then again for two hours immediately prior to being imaged with a CT scanner (Aquilone One, Toshiba). The vertebrae were oriented with the vertical axis aligned with the CT bore, then imaged using a skull reconstruction kernel (Brain HCT 1 mm Tremor [1], [2]) with an in-plane resolution of 0.503 mm and a slice thickness of 0.5 mm. Semi-automatic spine segmentation was performed using ITK-SNAP to generate 3D binary masks representing the individual vertebrae [43], then an open source mesh-generating algorithm (ISO2MESH) was used to generate mesh representations ($(\lambda/6)^2$ discretization) of the vertebral surfaces from the 3D binary masks [44]. The discretization is based on our previous validated model [11]. The vertebra meshes and corresponding CT data were aligned using rigid transformations such that each vertebra canal was centered in the horizontal plane at the origin, with the inferior and superior vertebral body surfaces aligned parallel to the horizontal plane. The individual vertebrae were then stacked $in\ silico$ in the neutral spine position, separated by vertebra-specific disk heights [42]. The acoustic properties of the vertebrae were assigned on a voxel-wise basis using the CT data and known CT intensity - acoustic property relationships derived from skull bone [10], [24] and interpolated to 500 kHz and extrapolated to 250 kHz.

2) Multi-layered Ray Acoustics: A previously validated multi-layered ray acoustics model for longitudinal and shear transvertebral ultrasound propagation was used to simulate acoustic propagation via the transvertebral path [11], and the Rayleigh integral [38] was used to simulate acoustic propagation via the paralaminar path. This model does not account for reflection from the anterior surface of the vertebral canal; the accuracy of this approximation when predicting maximum pressure distributions in the vertebral canal due to short pulses is described in [11], and short pulses have been shown to reduce standing wave formation in the vertebral canal, improving focal control [34]. The multi-layered ray acoustics model accounts for bone and accompanying acoustic parameter heterogeneity at the bone interfaces and in transvertebral propagation. The acoustic model is described with mathematical detail in the appendix. An NVIDIA GeForce GTX 1060 6GB GPU was used to compute the ray acoustics simulations. Simulation systems were limited to three stacked vertebrae (T1-T3, T2-T4, ... T10-T12) at a time to minimize computational cost while retaining the overlapping structure of the spine.

3) Backward Acoustic Simulation (Virtual Source): A 500 kHz source was placed at the center of the vertebral canal (horizontal plane), and a semi-cylindrical 'measurement' surface (12 cm radius, $\theta \in [-\pi/3, \pi/3]$) was placed 12 cm posterior to the source. The intervening propagation medium was given the acoustic properties of water (density: 994.04 kg/m^3, longitudinal speed of sound: 1482.2 m/s, longitudinal attenuation: 0.025 Np/m/MHz [23]) , making the assumption that the spine, not intervening soft tissue, is the primary source of wavefront aberration. Fig. 2 shows an example of the backward acoustic simulation system. Velocity propagation from the source to the measurement surface was calculated for the paravertebral and transvertebral paths. The source and measurement surface were translated in 1 mm increments in the vertical direction from the top to the bottom of the thoracic region of the spine, repeating the backward simulation with each increment. 300 increments were tested, spanning 30 cm. The effect of soft tissue attenuation was investigated by entirely replacing water with muscle (density: 1090.4 kg/m^3, longitudinal speed of sound: 1588.4 m/s, longitudinal attenuation: 7.1088 Np/m/MHz [23]).

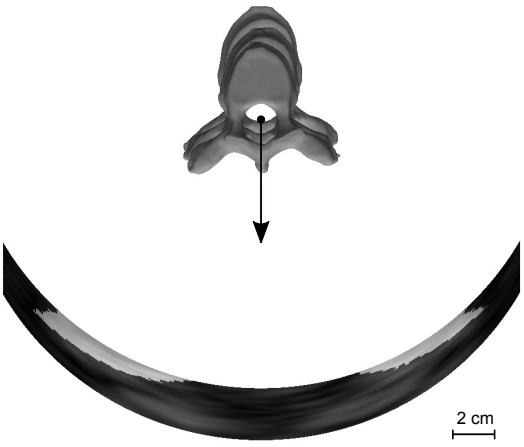

Fig. 2. Acoustic simulation with a source located within the canal, propagating via paravertebral and transvertebral paths towards a semi-cylindrical surface placed 12 cm posterior to the spine.

4) Array Element Positioning: The 2- and 4-component arrays were designed using the backward ray acoustics results and using a method analogous to subtractive manufacturing. For the 4-component array, element locations within the two paravertebral components were generated from the mean paravertebral velocity magnitudes in the measurement surface, and element locations within the two translaminar components were generated from the mean transvertebral velocity mag-

nitudes in the measurement surface. The mean normalized velocity magnitude ($|\overline{v}|$), at each discrete point (r_i), $\overline{|v(r_i)|}$ within the measurement surface was calculated as:

$$\overline{v(r_i)} = \frac{1}{M}\sum_{m=1}^{M}\frac{|v_m(r_i)|}{\overline{|v_m|}} \quad (1)$$

where $M = 300$ is the number of measurement surfaces and $\overline{|v_m|}$ is the mean velocity magnitude in measurement surface m. This approach was taken to avoid biasing the element positions towards generating arrays optimized for target locations that are relatively easy to sonicate, in favour of generating arrays equally optimized for any target spanning the thoracic region of the spine. The element placement algorithm for the 4-component array was as follows:

I) Average the paravertebral & transvertebral velocity magnitude surfaces across the mid-line to obtain lateral symmetry.
II) Place central elements at the paravertebral & transvertebral maximum velocity magnitude locations on left & right sides.
III) Pack >64 elements hexagonally (7.5 mm spacing) on the cylindrical surface around each central element.
IV) Calculate the velocity magnitude (efficiency) pertaining to each element.
V) Remove the least efficient elements until 64 remain in each component.

Element locations within the 2-component array were generated from the mean magnitude of the sum of the complex paravertebral and transvertebral velocity surfaces (Eq. 1). The element placement algorithm was as follows:

I) Average the combined velocity magnitude surfaces across the mid-line to obtain lateral symmetry.
II) Place central elements at the maximum magnitude of the combined velocity locations on left & right sides.
III) Pack >128 elements hexagonally (7.5 mm spacing) on the cylindrical surface around each central element.
IV) Calculate the velocity magnitude (efficiency) pertaining to each element.
V) Remove the least efficient elements until 128 remain in each component.

5) Forward Acoustics Simulation: The efficiencies and focal dimensions generated by the 2- and 4-component phased arrays were evaluated using forward multi-layered ray acoustics simulation. We define array efficiency as the target pressure in the vertebral canal, normalized by the target pressure in a water-only simulation system. We use the defined efficiency ratio in lieu of direct pressure or focal gain, as it combines spine-induced insertion loss with array beamforming accuracy in focusing to the intended target. The implemented multi-layered ray acoustic model allows retroactive pressure scaling or the calculation of the array power necessary to generate a desired $in\ situ$ pressure. We use pressure instead of intensity, as pressure is the relevant parameter for non-thermal treatments [5]–[7], and as intensity and corresponding heating is not of concern for the pressures and low duty cycle pulse sequences used in these non-thermal treatments. We obtain focal dimensions using the Matlab `isosurface` function, then ISO2MESH `finddisconnsurf` to find then isolate the primary focus from the secondary foci, then report the mean and standard deviation in primary focus dimensions (axial, lateral, vertical) for a set of targets. We tested 300 targets centered in the vertebral canal, spanning the height of the thoracic region of the spine (30 cm, 1 mm increments). The arrays were translated vertically for each target, and we tested sonication at 500 kHz and 250 kHz. We tested array steering (±5 mm lateral, 5 mm posterior) within the vertebral canal at each vertical positions with 500 kHz, as the larger dimensions of the 250 kHz foci were expected to limit the need for beam steering at in the canal at 250 kHz. An example of the target locations is displayed in Fig. 3. Ray tracing-based

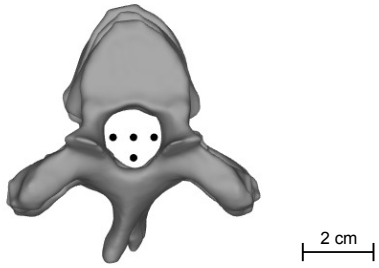

Fig. 3. Array aberration correction was tested using a central target in the vertebral canal and electronic steering was tested with three targets lateral (±5 mm) and posterior (5 mm posterior) to the central target. 300 vertical locations were tested, spanning 30 cm in the thoracic region of the spine.

beamforming [40] was used to correct for vertebra-induced aberration and for lateral and posterior steering within the canal. Ray tracing was used in order to avoid using the same propagation model and assumptions for both beamforming and subsequent forward simulation. In ray tracing, the complex velocity v of the i^{th} array element is given by:

$$v_i = \exp\left[j\omega\int_{r_{\text{focus}}}^{r_i}\frac{dr}{c(r)}\right] \quad (2)$$

where r_i the spatial location of the i^{th} array element, r_{focus} is the spatial location of the intended focus, $c(r)$ is the speed of sound at location r, and dr is an infinitesimal distance along the direct path between r_i and r_{focus}. Phase conjugation of v was implemented for phase correction [40], and we did not implement amplitude correction [45] as we wished to determine total array efficiency without biasing the results by prioritizing propagation via single elements within the arrays. For the two paravertebral components of the 4-component array, $c(r)$ is the speed of sound in the intervening propagation medium, for all r. For the two translaminar components of the 4-component array, $c(r)$ is given by the CT density - longitudinal speed of sound relationship described in [10] for r within bone, otherwise the speed of sound in the intervening propagation medium. In the 2-component array, a ray was traced from r_{focus} to r_i. If the ray transects bone, the element propagated via the translaminar path, if the ray remains in water, the element propagated via the paravertebral path. Acoustic pressure was calculated using the ray acoustics model within a 16 mm x 16 mm x 16 mm volume (0.5 mm discretization) centered at the target location. Acoustic pressure was also calculated in a paraspinal volume (10 mm to 40 mm posterior to the target,

-40mm to 40mm lateral to the target, and -40mm to 40mm in the vertical direction relative to the target, 1 mm discretization) in a subset of 30 simulations vertically centered within the T4-T6 canal to compare the target/paraspinal pressure ratio generated by the arrays to the simulated and experimentally measured ratios in [11]. Pressure transmitted directly from the arrays and pressures reflected from vertebral surfaces to the paraspinal volumes were calculated independently then summed, allowing for an approximate differentiation between the expected paraspinal pressures generated using short pulses and those generated with continuous sonication.

The majority of the simulations were performed with thoracic vertebrae stacked in the neutral position; the worst-case scenario wherein a patient is incapable of spine flexion to increase the paravertebral spaces. The majority of the analysis was performed on arrays focused to targets centered in the vertebral canal. A two-tailed two-sample t-test (`ttest2`) was performed on the focal pressures of the 4-component and 2-component arrays to determine if there is a statistically significant difference between array efficiencies. The forward simulations were repeated with 10° of sagittal flexion in the sets of three stacked vertebrae. 10° is near the physiological limit for spine flexion between three thoracic vertebrae, and intermediate degrees of flexion are expected to provide intermediate array efficiency improvement. A one-tailed two-sample t-test was performed on the focal pressures in the neutral and flexed spines for both arrays to determine if sagittal flexion improves array efficiency. A re-configurable array, where components can be translated relative to each another, may further improve array efficiency. We tested this idea, using backward acoustic simulation to place each of the four components of the four component array in target-specific positions to maximize path-specific efficiency (without component overlap). A one-tailed two-sample t-test was performed on the focal pressures of the fixed 4-component and re-configurable 4-component array to determine if array re-configuration improves array efficiency. The majority of the analysis was performed with the intervening propagation medium treated as water. However, we tested the effect of soft-tissue attenuation at 500 kHz (neutral spine) by entirely replacing water with muscle (no water-muscle interface), as was done in the backward acoustic simulation. Muscle is a relatively highly attenuating soft tissue, and by treating the entire intervening volume as muscle, we aimed to provide an upper limit on soft-tissue based pressure loss.

We tested array steering (up to 5 cm in the array's axial, lateral, and vertical directions) in water to determine the array steering capabilities, as array steering will be necessary for focusing through the backs of patients with varying intervening soft-tissue volumes. We also anticipated the arrays to form secondary foci due to the expected dual aperture of the spine-specific phased arrays [46], along with the regularly spaced elements with dimensions exceeding $\lambda/2$. These secondary foci can be partially mitigated using pulse design [34], [47]. However, the multi-layered ray acoustics method we implemented only treats linear continuous wave sonication. Instead, we evaluated array electronic focusing in water using short pulses using the k-Wave toolbox (`kspaceFirstOrder3DG`, spatial resolution 0.5 mm isotropic, temporal resolution 5e-8 s, uniform maximum source velocity magnitude 1 m/s) [48]. Specifically, we calculated pressure at the focus and pressure in the anticipated secondary foci. We simulated two driving signals (Fig. 4): continuous 500 kHz, and the response of a spherically focused (f-number 1.2) piezocomposite transducer (DeL Piezo Specialties, LLC, West Palm Beach, FL, USA) assembled in house, driven with a single 500 kHz sinusoidal cycle (Function Generator: Tektronix AFG3052C, Amplifier: NP Technologies model NP-2519), measured at the focus with a 0.5 mm needle hydrophone (Precision Acoustics).

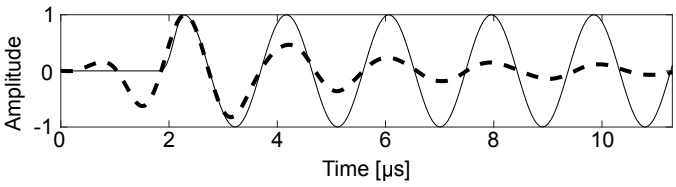

Fig. 4. Array steering was tested with each element driven at 500 kHz: continuously (black), and with a short pulse (grey dashes).

III. Results

Backward acoustic simulation was performed with virtual sources spanning the height of the thoracic region of the spinal cord, propagating through the spine to corresponding semi-cylindrical surfaces placed 12 cm posterior to each source. The full set of simulations were performed at 500 kHz and repeated at 250 kHz. The cylindrical velocity measurement surface is projected to a plane for visualization in Fig. 5, with the average total velocity magnitude, paravertebral velocity magnitude, and transvertebral velocity magnitude displayed. Fig. 5 demonstrates that the paravertebral and transvertebral velocity magnitude fields are spatially distinct. The velocity magnitude fields are laterally asymmetrical due to lateral asymmetries in the spine. During array design, we assumed the average human spine is laterally symmetric. The spatial pressure distributions of the 500 kHz and 250 kHz velocity magnitude fields were similar, although the spatial distribution of the transvertebral field was more tightly defined at 500 kHz, leading to our use of the 500 kHz fields for array design. The mean velocity magnitude field shown in Fig. 5a) was used to position the elements in the 2-component array, and the mean velocity magnitude fields shown in Fig. 5b) and c) were used to position the elements in the paravertebral components and translaminar components of the 4-component array. Array elements and rays traced from the focus to the elements are displayed in Fig. 6 for the 4-component and 2-component arrays. An identical set of simulations at 500 kHz was performed with muscle in lieu of water. Once normalized (Eq. 1), the maximum muscle-water difference in mean velocity magnitude at the measurement surface was $<10\%$, with a slight bias towards measurement surface locations that minimize the target-surface distance. These locations were precedently populated by elements, meaning that the end array designs (Fig. 6) were unchanged.

Fig. 7 shows an example of the simulated pressure profiles generated by the arrays focused to a target at the centre of

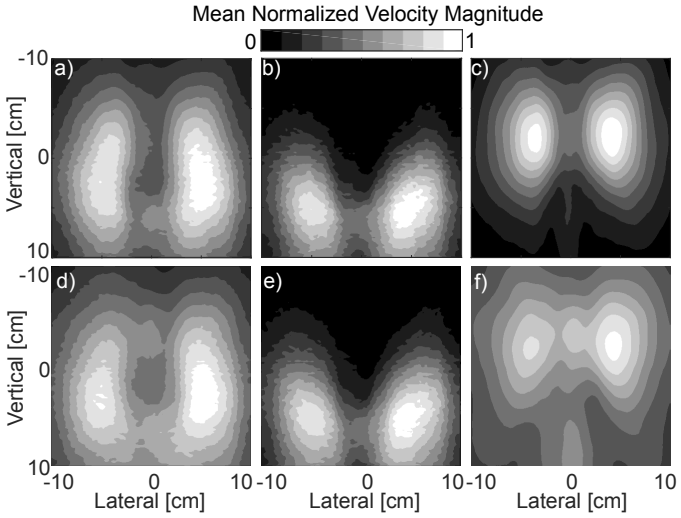

Fig. 5. Transspine posterior velocity propagation: (a,d) Total velocity magnitude field (b,e) Paravertebral velocity magnitude field (c,f) Transvertebral velocity magnitude field. Velocity magnitude fields are projected from a cylindrical surface to a planar surface for visualization, and contour levels are in 10% increments. Top row (a,b,c): 500 kHz; Bottom row (d,e,f): 250 kHz.

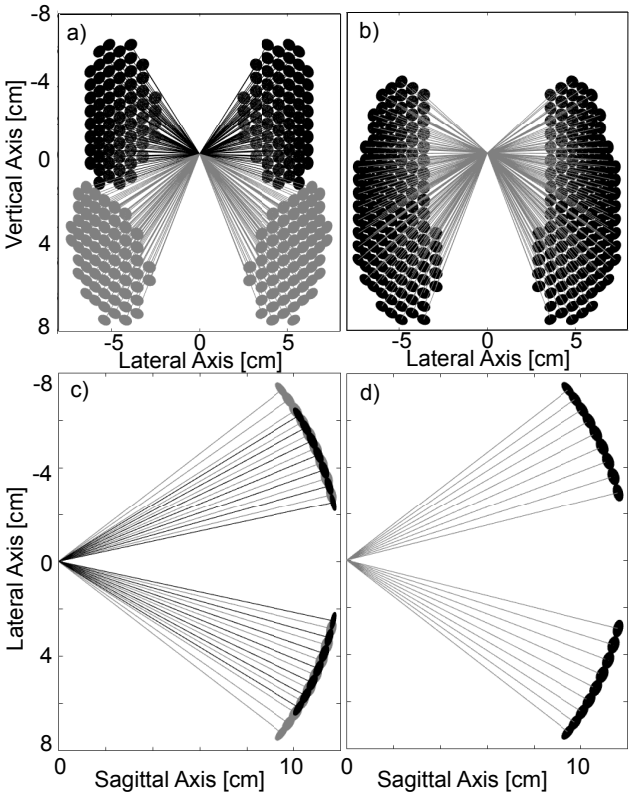

Fig. 6. Transspine array designs: Anterior (a,b), and superior (c,d) views of the 4-component array (a,c) and the 2-component array (b,d), with rays traced from the origin/focus to the elements. The translaminar elements in the 4-component array are displayed in black, while the paravertebral elements in the 4-component array are displayed in grey.

the vertebral canal. These simulations were performed for 300 targets per array to calculate array efficiency and mean focal dimensions. Fig. 7 shows the placement of the arrays relative to the spine (Fig. 7a) and d), the focal locations relative to the arrays, and expanded views of the pressure profiles within the vertebral canal (Fig. 7b) and c) for the 4-component array, e) and f) for the 2-component array).

Fig. 8a) shows a subset of the targets centered in the vertebral canal spanning T3 to T5. The sound transmission via the paravertebral and transvertebral paths varies by vertical position (Fig. 8b). Bony occlusion results in variance in paravertebral transmission efficiency, and the combination of occlusion and focal distortion results in variance in the efficiency of the arrays. For example, focal distortion may result in spatial shifts between the maximum pressure location and the target location, resulting in a decrease in efficiency. The distributions of focal shifts ($\overline{\Delta R}$) are reported in Table IV for central and steered targets. The mean and variance in array efficiency is displayed for the arrays by set of three thoracic vertebrae in Fig. 8c).

Fig. 8 displays the array efficiencies for central targets. The results are separated into groups of three neutral thoracic vertebrae in Fig. 8. Table I and II report the total mean and standard deviations in array efficiencies for both arrays (500 kHz & 250 kHz), for central targets, for neutral and flexed spines, and for the re-configurable 4-component array. The difference between array efficiencies are statistically significant ($p < 1e{-}3$), and the focal pressures of the re-configurable 4-component array were significantly higher than those of the fixed 4-component array ($p < 1e{-}10$). Sagittal spine flexion ($p < 1e{-}10$) and 4-component array re-configuration both improved mean transspine propagation efficiency by approximately 24% relative to neutral for the 4-component array, although flexion did not significantly improve 2-component array efficiency ($p = 0.23$). The efficiency improvement varied strongly by target for spine flexion, but re-configuration resulted in consistent improvement, as reported by the standard deviations in array efficiencies in Table I.

TABLE I
MEAN TRANSSPINE FOCAL CHARACTERISTICS (500 KHZ)

500 kHz Array & Spine Position	50% pressure dimensions [mm]			Efficiency [%]
	Axial	Lateral	Vertical	
4-comp., water	16.2	2.5	4.0	100
4-comp., neutral	10.8 ± 2.7	4.2 ± 2.7	5.9 ± 2.1	29 ± 13
4-comp., flexed	11.5 ± 2.2	3.5 ± 1.7	6.2 ± 2.1	36 ± 18
4-comp., neutral (reconfigurable)	12.6 ± 2.0	5.3 ± 2.4	8.7 ± 3.5	36 ± 8
4-comp., neutral (muscle)	11.2 ± 2.4	4.2 ± 2.7	5.2 ± 1.8	21 ± 9
2-comp., water	18.4	2.3	5.2	100
2-comp., neutral	11.9 ± 2.4	5.6 ± 3.0	6.2 ± 2.0	32 ± 11
2-comp., flexed	12.5 ± 2.2	4.7 ± 2.9	6.5 ± 2.2	33 ± 15
2-comp., neutral (muscle)	12.2 ± 2.2	5.2 ± 3.1	6.0 ± 1.9	25 ± 9

Focal characteristics of the 4- and 2-component phased arrays at 500 kHz: 50% pressure dimensions and efficiency (focal pressure in canal vs. water).

Pressure in the intervening paraspinal medium was calculated for a subset of 30 targets vertically centered within the T4-T6 canal. The simulations were performed with the

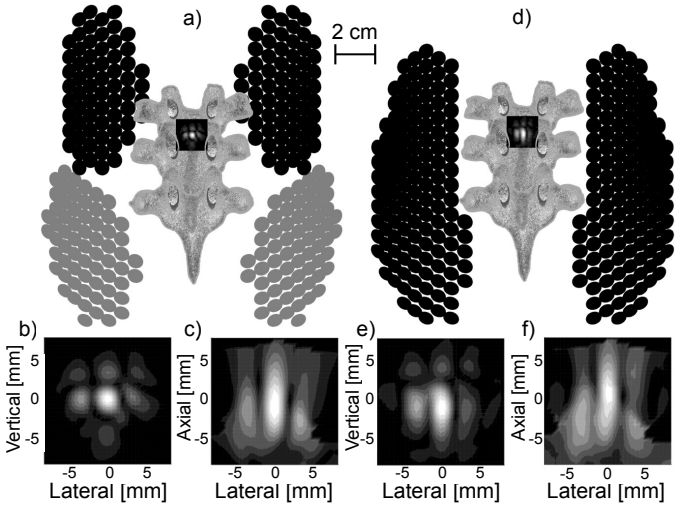

Fig. 7. Forward simulation with the (a) 4- and (d) 2-component phased arrays focused to a target at the centre of the vertebral canal. (b) and (e) are anterior views of the focal pressure profiles, while (c) and (f) are superior view of the focal pressure profiles (normalized: black = 0, white = 1).

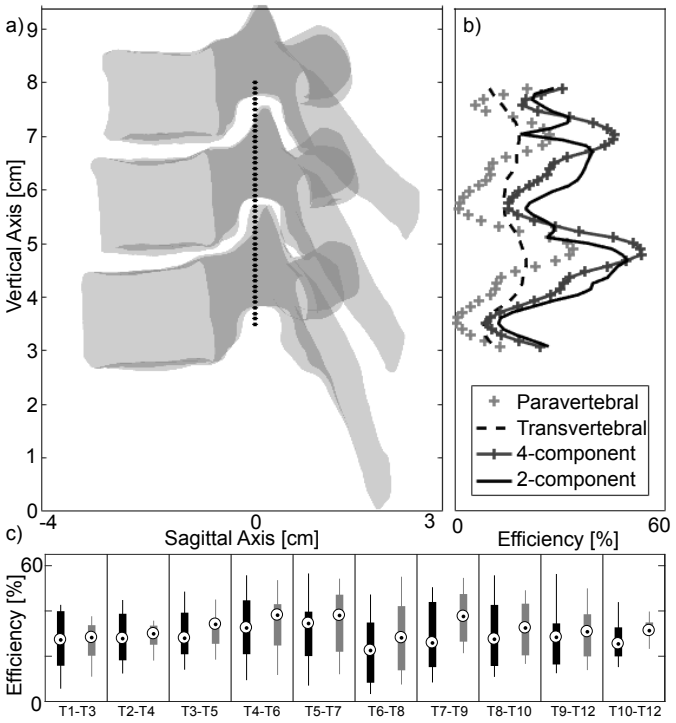

Fig. 8. a) Vertical target locations centered in the vertebral canal between T3 - T5. b) Corresponding 2- and 4-component array efficiency, along with the paravertebral and transvertebral contributions to the 4-component array efficiency. The vertical axes of a) and b) are identical. c) Box plots of array (black: 4-component, grey: 2-component) efficiency by group of three stacked thoracic vertebrae. The circles depict median efficiency, the thick lines depict the interquartile range, and the thin lines extend to the most extreme points.

paraspinal medium treated as water, for comparison with [11], and as muscle, to account for soft-tissue attenuation expected *in vivo*. Table III reports the ratio of focal pressure to the maximum acoustic pressure a) directly transmitted from the array to the paraspinal medium, b) reflected from the spine surface back to the paraspinal medium, and c) the combination of reflected and direct pressure.

TABLE II
MEAN TRANSSPINE FOCAL CHARACTERISTICS (250 KHZ)

250 kHz Array & Spine Position	50% pressure dimensions [mm]			Efficiency [%]
	Axial	Lateral	Vertical	
4-comp., water	33.1	5.1	8.2	100
4-comp., neutral	12.7 ± 2.5	7.9 ± 3.6	7.9 ± 2.7	36 ± 13
2-comp., water	37.6	4.7	10.6	100
2-comp., neutral	13.1 ± 2.7	9.5 ± 4.2	8.5 ± 2.4	43 ± 17

Focal characteristics of the 4- and 2-component phased arrays at 250 kHz: 50% pressure dimensions and array efficiency (pressure in canal vs. water).

TABLE III
TARGET/PARASPINAL PRESSURE RATIO (500 KHZ)

500 kHz Array & Medium	Target/Paraspinal Ratio		
	Direct	Reflected	Total
4-comp., water	1.85 ± 0.57	2.45 ± 0.74	0.93 ± 0.29
4-comp., muscle	1.87 ± 0.57	3.05 ± 0.93	0.99 ± 0.32
2-comp., water	1.27 ± 0.27	1.93 ± 0.48	0.91 ± 0.19
2-comp., muscle	1.28 ± 0.29	2.32 ± 0.55	0.97 ± 0.25

The ratios of target to maximum paraspinal pressures (direct from the arrays, reflected from the spine, total sum of direct and reflected) for the 2- and 4-component arrays in water and in muscle.

Fig. 9 displays the average 50% maximum pressure contours for centered targets generated at 500 kHz and 250 kHz. The primary foci shown in Fig. 9 are ellipsoids with dimensions reported in Table I for 500 kHz and Table II for 250 kHz. The 250 kHz foci are truncated in the axial direction by the bounds of the vertebral canal, with small differences by array resulting from differences in focal dimensions when the focus is unbounded, i.e. at the level of the intervertebral disks. Fig. 9 shows that secondary foci exceeding 50% maximum pressure exist for targets centered in the vertebral canal. The secondary foci are caused by the dual aperture nature of the arrays in addition to the continuous-wave nature of the simulated sound transmitted through the vertebrae. Other studies have shown that multi-frequency [47] or phase-keyed pulses [34] can mitigate these grating lobes to produce a larger but more uniform main lobe.

The 2- and 4-component arrays were steered laterally at 500 kHz ($\pm$5 mm) and 5 mm in the posterior direction inside the vertebral canal. Fig. 10 displays the average steered 70% maximum pressure contours, and the array steering efficiencies are reported in Table IV. 70% contours were used to visualize the foci due to increased side-lobe prevalence (quantified in Table IV). Fig. 10 shows that two focal lobes appear when steering laterally; one at the intended location of the focus, one medial and the result of constructive interference between the left and right beams. Table IV reports the ratio (p_{tgt}/p_{max}) of the pressure at the target (p_{tgt}) to the maximum pressure in the canal (p_{max}), along with the mean distance between the target and the maximum pressure location, $\overline{\Delta R}$.

Array steering in a water-only medium was tested using simulation in k-Wave, allowing for time-varying sources to

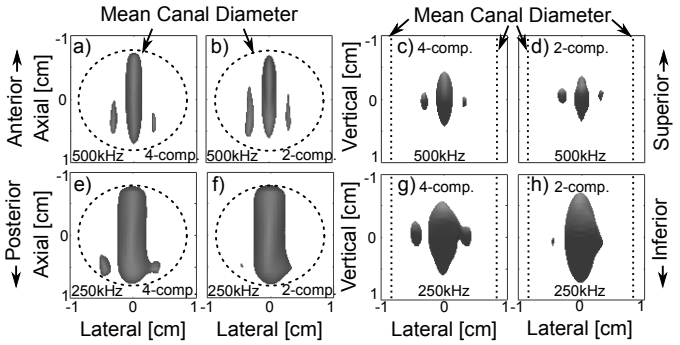

Fig. 9. Superior (a,b,e,f) and anterior (c,d,g,h) views of the mean foci (50% pressure contours) produced by the 4-component (a,c,e,g) and 2-component array (b,d,f,h) focused to targets in the center of the vertebral canal, spanning the thorax. The top row (a,b,c,d) and bottom row (e,f,g,h) correspond to 500 kHz and 250 kHz respectively. Dashed lines represent mean thoracic canal dimensions [42].

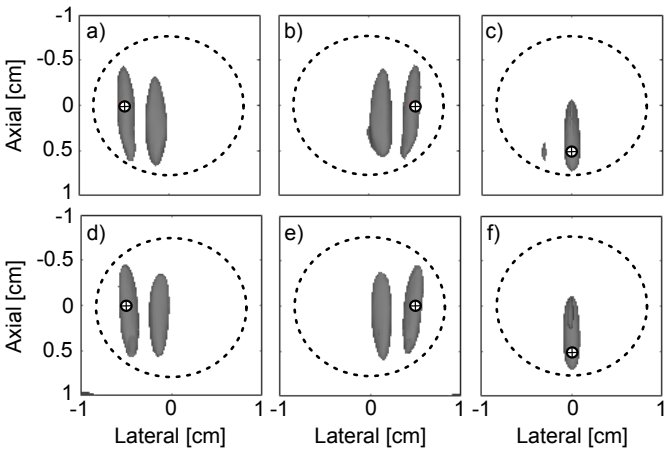

Fig. 10. Superior views of the mean foci (70% pressure contours) produced by the 4-component (a,b,c) and 2-component array (d,e,f) focused to targets steered 5 mm left (a,d), 5 mm right(b,e), and 5 mm in the posterior direction (c.f). The $\oplus$ markers denote the target locations. Dashed lines represent mean thoracic canal dimensions [42]

be simulated. Fig. 11 reports the primary and secondary focal pressures for both arrays steered ± 5 cm sagitally, laterally and vertically. Continuous sonication and a short pulse (Fig. 4) were both simulated, and short pulses produced substantial decreases $(20 - 40\%)$ in secondary focus amplitude in the 6 cm^3 volume centered at the geometric focus of both arrays.

IV. Discussion

We designed two spine-specific arrays; one with four path-specific components, the other with two laterally symmetric components. The 4-component array was designed using the average thoracic ultrasound propagation from 500 kHz virtual sources through the separate paralaminar (Fig. 2b) and translaminar (Fig. 2c) paths, and the 2-component array was designed using total transspine ultrasound propagation (Fig. 2a). Backward propagation at 250 kHz and through muscle in lieu of water both produced similar spatial patterns to backward propagation at 500 kHz, although the spatial distribution of the transvertebral velocity field was less spatially distinct at 250 kHz as a result of lower attenuation and the resultant

TABLE IV
Array Steering (Canal)

Array Steering	Efficiency [%]	p_{tgt}/p_{max} [%]	$\overline{\Delta R}$ [mm]
4-comp., center	29 ± 13	73 ± 19	1.8 ± 1.9
4-comp., right	12 ± 7	42 ± 16	4.8 ± 2.9
4-comp., left	13 ± 7	45 ± 20	4.7 ± 2.7
4-comp., post.	21 ± 15	59 ± 27	1.7 ± 1.6
4-comp., center (250 kHz)	36 ± 13	69 ± 19	3.8 ± 2.7
2-comp., center	32 ± 11	85 ± 15	1.6 ± 2.0
2-comp., right	13 ± 4	38 ± 15	5.5 ± 3.3
2-comp., left	16 ± 5	45 ± 16	4.6 ± 2.7
2-comp., post.	23 ± 11	66 ± 22	2.3 ± 1.8
2-comp., center (250 kHz)	43 ± 17	75 ± 18	3.6 ± 2.7

Focal characteristics for 4- and 2-component phased array steering: efficiency (focal pressure, normalized by focal pressure in water), the ratio of average focal pressure to maximum canal pressure (p_{tgt}/p_{max}), and the distance between target and maximum pressure location ($\overline{\Delta R}$).

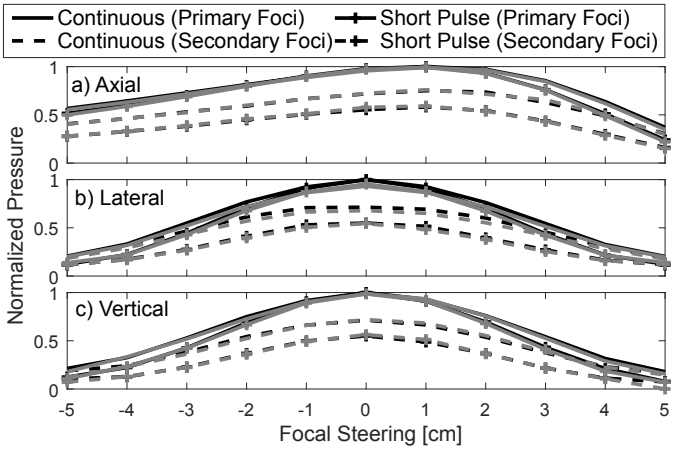

Fig. 11. Focal steering in water with the 4-component array (black) and 2-component array (grey) driven continuously vs. driven with a short pulse. a) axial steering, b) lateral steering, c) vertical steering. Solid lines represent the primary foci, dashed lines represent secondary foci.

increase in available transvertebral paths, and there was a slight bias towards shorter path lengths in the muscle simulations. Fig. 2 shows that the two velocity magnitude fields are spatially distinct, providing the motivation for the design of the 4-component array with distinct paralaminar and translaminar components. The vertical spatial footprint of the 4-component array is slightly larger than that of the 2-component array due to bias towards paravertebral transmission (Fig. 6), but both have the same dual aperture shape; demonstrating that ultrasound transmission along the midline (through the spinous processes) is inefficient. We implemented a spine-specific adaptive beamforming algorithm for the 2-component array to determine which approach (dedicated components vs. adaptive beamforming) is most efficient.

We used forward simulation to test array efficiency at 500 kHz for targets centered in the vertebral canal. The forward simulation model is based on ray acoustics, assumes continuous sonication, and implements a simple ray-tracing

based algorithm for phase correction beamforming [40]. We tested two additional ideas hypothesized to improve array efficiency: sagittal spine flexion and 4-component array re-configuration. Forward simulation (e.g. Fig 8b) shows that the paralaminar path is ineffective for certain levels (targets at the vertical height of the center of the vertebral bodies), but highly effective for others (targets at the vertical levels of the superior & inferior surfaces of the vertebral bodies). The 2-component array achieved higher average transspine propagation efficiency in the neutral spine position; primarily due to the adaptive focusing algorithm, capable of re-purposing elements occluded from the paravertebral route to propagate via the translaminar path instead. However, the 4-component array achieved higher average transspine propagation efficiency in the flexed position, where the larger paravertebral spaces increased the opportunities for paravertebral propagation. The 2-component array efficiency showed negligible improvement with spine flexion, perhaps because spine flexion increases the spatial separation of the para- and transvertebral pathways, and the vertical extent of 2-component array is too small to efficiently exploit the increased paralaminar space. Re-configuring the 4-component array for specific targets increased transspine propagation efficiency an equal amount to flexing the spine. This suggests that increasing the array footprint by adding elements to the arrays could similarly improve transspine propagation efficiency. The combination of spine flexion and array re-configuration could also further improve transspine propagation efficiency. We tested array focusing with 250 kHz, as lower frequencies are less attenuated [10], [24] and less susceptible to aberration and found that efficiency improved for both arrays at the expense of nearly doubling the lateral dimensions of the foci (Fig. 9, Table II).

Forward simulation with muscle as the intervening medium showed that soft tissue-based attenuation decreases efficiency by an additional 7-8% relative to the water-spine system. This represents a limiting case, where the entirety of the intervening medium is muscle; in an average patient, the path length through muscle will be half that which was simulated here [36]. Microbubbles, commonly used ultrasound contrast and therapy agents [5], [6], [16], [49], provide an additional attenuative mechanism, and a form of amplitude correction [45] may be required in practice to compensate for the path-dependent attenuation for each element. The simulation system approximates the multiple soft tissue layers in the thorax (skin $\rightarrow$ fat $\rightarrow$ muscle $\rightarrow$ tendon & ligament $\rightarrow$ spinal cord & cerebrospinal fluid), approximating them as homogeneous medium and making the assumption that the spine is the primary source of waveform aberration. Ray acoustics models incorporating multiple soft tissue layers have been implemented [50], [51] and may be incorporated for patient-specific beamforming through both spine and surrounding soft tissues.

Pressure in the paraspinal region was calculated for a subset of targets surrounding T5 for comparison to the canal/prelaminar pressure ratio simulated (0.48) and experimentally measured (0.55) in [11]. Table III shows that 2- and 4-component arrays nearly double the ratio for continuous sonication, with further improvements for pulsed sonication where sound directly transmitted from the array and sound reflected from the spine is temporally distinct. Simulation with muscle in lieu of water demonstrated further improved target/paraspinal pressure ratios, due to the lower impedance mismatch of the muscle-spine system. The target/paraspinal pressure ratio in non-thermal treatments such as blood-spinal cord barrier opening is less important than for thermal treatment, where bone and paraspinal tissue heating may be unsafe. However, microbubble-induced hemorrhage in the paraspinal region during non-thermal treatment is possible if the target/paraspinal pressure ratio is low, making the demonstrated improvement in this ratio important for clinical translation.

The differences in focal volume dimensions (central targets) between the two arrays are insignificant, and the focal volumes are similar in neutral and flexed spines, and with muscle in place of water. As expected, the 250 kHz lateral focal volume dimensions were larger than those at 500 kHz, and similar in size to the lateral dimensions of the spinal cord [52]. Therefore, 250 kHz may be suitable for sonicating the entire width of a spinal cord segment without the need for electronic intra-canal steering. Both arrays are capable of producing a controlled focus at the center of the canal within the thoracic region of the spine. The mean FWHM dimensions for central targets (Fig. 9, reported in Tables I and II) show that the axial focal dimensions are slightly larger than mean spinal cord diameter in the anterior/posterior direction [52], but smaller than the diameter of the canal [42] due to bone shielding and the high degree of canal curvature acting as a focusing lens. If necessary, the array's axial FWHM may be decreased by increasing the angular separation of the array components or using short pulses [34]. The vertical FWHM is of lesser concern given the vertical continuity of the spinal cord tracts. The lateral FWHM at 500 kHz is sufficiently small that it may be possible to target individual funiculi or the grey matter horns, but not individual tracts within the spinal cord.

The intra-canal 500 kHz steering results are less promising. Fig. 10 and Table IV showed that lateral steering decreases array efficiency, and the arrays produce high pressure lobes medial to the target focus; the result of constructive interference between ultrasound beams from the left and right array components. We found that the pressure at the lateral targets tended to be lower than in the medial lobe. Short pulses and time-domain beamforming may improve the focal pressure to medial pressure ratio [30], [31], [34], [53]; testing this requires a different forward simulation model and improved beamforming [48], [54]. Posterior steering decreased efficiency, primarily due to bone shielding by the overlapping spinous processes. Both arrays produced coherent foci neatly located at the intended posterior target locations.

Array steering (up to 5 cm in the axial, lateral, and vertical directions) was also simulated in water at 500 kHz to determine the array translations that permit coherent foci formation. Fig. 11 shows that primary focal pressure remains $>$90% for 1 cm steering in all directions, which is sufficient given the $\sim$1 cm radius of the vertebral canal, and particularly if the array is vertically mechanically translated for targets at different vertical locations. Steering in the array's axial direction shows that focal pressure is well maintained ($>$75% maximum) for a range of $\pm$3 cm, giving the arrays some flexi-

bility for treating larger patients. A planar, fully electronically steerable array (e.g. [55]) may be better suited for patients exceeding the steering threshold of the spine-specific arrays, at the expense of electronic complexity. Further pulse design (e.g. frequency differences and/or short pulses & phase shift keying) can be implemented to temporally smooth the focus over a set of pulses [34], [46]. k-Wave simulations were not used for transspine focusing due to memory constraints - avoiding significant simulation error due to staircasing requires simulation domains that exceed the memory constraints of the GPU used for this work.

A limitation of the multi-layered ray acoustic model is that it does not account for multiple reflections and consequent waveform decoherence that may occur in the paralaminar space (Fig. 1) However, multiple reflections can be implemented in the future, and we believe the limitations of the multi-layered ray acoustics model are justifiable as spine-specific array design is primarily a geometrical acoustics problem, and the associated low computational cost enabled us to perform the large sets of simulations required to design and test the spine-specific arrays. Future work with full wave simulation and improved beamforming may improve array performance, given the limited accuracy of ray-tracing [30], [31], [53]. Future $ex\ vivo$ work in a human spine will be performed to validate the simulation results presented in this work, then $in\ vivo$ experiments in a porcine model, a clinically-relevant large animal model [42], will be performed to demonstrate safe, targeted blood-spinal cord barrier opening.

V. Conclusion

The geometry of the thoracic region of the spine indicates two paths for transspine ultrasound: through acoustic windows between vertebrae (paravertebral path), and through the bone itself (translaminar path). We designed and tested two 500 kHz multi-component arrays using multi-layered ray acoustics simulation; a 4-component array with dedicated components for the paravertebral and transvertebral paths, and a laterally symmetric 2-component array where the propagation path of each element is determined using adaptive focusing. Forward simulation shows that 4-component array maximizes transspine propagation efficiency for targets accessible via the paravertebral path, but that adaptive focusing maximizes mean transspine propagation to evenly-spaced targets vertically spanning the thoracic region of the spine. Forward simulation showed that sagittal spine flexion (10°) and target-specific re-configuring of the 4-component array independently significantly increased transspine propagation efficiency. Forward simulation at 250 kHz with the same arrays also improved array efficiency, although at the expensive of producing loosely defined foci. Both multi-component arrays produce controlled foci located within the vertebral canal, a crucial step towards the clinical translation of focused ultrasound for the treatment of spinal cord disease.

Appendix
Ray Acoustics Model

Ray acoustics is used to calculate paravertebral and transvertebral ultrasound propagation. We begin with the simpler case, paravertebral propagation, where pressure p_l generated by M discrete acoustic sources is numerically approximated by the discretized form of the Rayleigh integral [38]:

$$p_L = \sum_{m=1}^{M} p_{L,m} = \frac{i\rho c_L k_L^*}{2\pi} \sum_{m=1}^{M} |\vec{u}_{L,m}| \frac{e^{i(\omega t - k_L^* r_m)}}{r_m} \Delta S_m, \quad (3)$$

where ρ and c_L are the respective density and longitudinal speed of sound of the local medium. In Eq. 3, ω denotes the angular frequency of the acoustics sources and $k_L^* = k_L + i\alpha_L$ is the complex longitudinal wavenumber of the medium within which the sources reside, where α_L is the corresponding attenuation coefficient. r_m is the magnitude of $\vec{r}_m$, the displacement vector of the target point from the mth source, $\vec{u}_{L,m}$ is the longitudinal particle velocity vector along the normal to the surface of the mth source, and ΔS_m is the area of the mth source [38], [39]. A binary mask-based occlusion test was implemented. The occlusion test propagates voxel-by-voxel along the paths between each source element and the target, checking each voxel on the path to determine if the medium changes. A change of medium is determined to have occurred if a point and its nearest neighbours in the mask are differ from the end points of the line segment. Sound is not propagated from source to target if a medium change is detected. Pressures may be scaled retroactively by assigning uniform velocities to the discrete acoustic sources representing the array $u_{L,m} = 1$ m/s, then calculating the direct pressure p_L^d resultant from an array power P using the following:

$$p_L^d = p_L \times \frac{2P}{\sum_{m=1}^{M} \Delta S_m c_L \rho} \quad (4)$$

Conversely, the array power required to generate a desired direct pressure can be obtained by rearranging Eq. 4.

Transvertebral ultrasound propagation accounts for the fluid-solid and solid-fluid interfaces between the acoustic sources and target. Sound transmitted to the vertebral canal via the transvertebral path results from the sum of purely longitudinal transmitted sound and converted sound from shear-mode transmission. The multi-layered ray acoustics model is based on velocity propagation through a medium. The longitudinal particle velocity, $\vec{v}_L$, at any point in a homogeneous inviscid medium due to M discrete acoustic sources may be numerically approximated by

$$\vec{v}_L = \frac{ik_L^*}{2\pi} \sum_{m=1}^{M} |\vec{u}_{L,m}| \left[1 - i\frac{1}{k_L^* r_m}\right] \frac{e^{i(\omega t - k_L^* r_m)}}{r_m} \Delta S_m \hat{r}_m. \quad (5)$$

Analogous expressions may be assumed for shear waves [56], and propagation of longitudinal and shear waves within a single medium are treated independently of one another [22].

Propagation of sound into a second medium is achieved by first discretizing the interface between media into finite planar elements, then independently approximating each summand in Eq. 5 as a plane wave. These plane waves undergo transmission at the interfacial element, with the resultant transmitted phases and magnitudes determined by transmission coefficient derived in [22], which satisfy the assumption of welded contact between the two media, as well as all shear waves being vertically polarized. Next, an approximation based upon Huygens' Principle is applied, wherein the sum of transmitted plane

waves impinging on an interfacial element is condensed into a new single hemispherical acoustic source. Only the particle velocity components of each plane wave normal to the surface element associated with the point are considered [39]. This is achieved by multiplying each transmitted velocity contribution by the cosine of its transmitted angle, although a change of mode, i.e. longitudinal to shear, or shear to longitudinal, requires multiplication by the sine of the transmitted angle instead, due to orthogonality. The equations for the transmitted longitudinal particle velocity, $\vec{v}_L$ and transmitted shear particle velocity $\vec{v}_S$ at a point on a surface representing a change of medium from a liquid to a solid are the following:

$$\vec{v}_L = \frac{ik_L^*}{2\pi}\sum_{m=1}^{M}\left\{\cos(\theta_m)T_{LL,m}\left|\vec{u}_{L,m}\right| \times\left[1-i\frac{1}{k_L^* r_m}\right]\frac{e^{i(\omega t-k_L^* r_m)}}{r_m}\Delta S_m\hat{r}_m\right\}, \tag{6}$$

$$\vec{v}_S = \frac{ik_L^*}{2\pi}\sum_{m=1}^{M}\left\{\sin(\theta_m)T_{LS,m}\left|\vec{u}_{L,m}\right| \times\left[1-i\frac{1}{k_L^* r_m}\right]\frac{e^{i(\omega t-k_L^* r_m)}}{r_m}\Delta S_m\hat{r}_m\right\}, \tag{7}$$

respectively. θ_m is the incident angle that the mth plane wave due to a longitudinal source makes with the surface element, and $T_{LL,m}$ and and $T_{LS,m}$ are the mth longitudinal and shear transmission coefficients, respectively. The equation for the transmitted longitudinal particle velocity at a point on a surface representing a change of medium from a solid to a liquid is

$$\begin{aligned}\vec{v}_L = &\frac{ik_L^*}{2\pi}\sum_{m=1}^{M}\left\{\cos(\theta_{L,m})T_{LL,m}\left|\vec{u}_{L,m}\right| \times\left[1-i\frac{1}{k_L^* r_m}\right]\frac{e^{i(\omega t-k_L^* r_m)}}{r_m}\Delta S_m\hat{r}_m\right\}\\ &+\frac{ik_S^*}{2\pi}\sum_{m=1}^{M}\left\{\sin(\theta_{S,m})T_{SL,m}\left|\vec{u}_{S,m}\right| \times\left[1-i\frac{1}{k_S^* r_n}\right]\frac{e^{i(\omega t-k_S^* r_m)}}{r_m}\Delta S_m\hat{r}_m\right\},\end{aligned} \tag{8}$$

where $\theta_{L,m}$ is the incident angle that the mth plane wave (longitudinal source) makes with the surface element, $\theta_{S,m}$ is the same but for shear waves, $T_{LL,m}$ is the mth transmission coefficient for a longitudinal source, $T_{SL,m}$ is the same but for shear sources, and $k_S^* = k_S + i\alpha_S$ denotes the complex shear wavenumber, where α_S is the shear attenuation coefficient. Backward paravertebral velocity propagation is calculated using Eq. 6. Backward transvertebral velocity propagation is calculated using Eqs. 6 and 7, then Eq. 8, then Eq. 6. In the forward acoustic simulation, pressure transmitted via the transvertebral path, p_L, is calculated using Eqs. 6 and 7, then Eq. 8, then Eq. 3. Reflections within the canal are not considered. The accuracy of this approach has been reported in [11] for short pulses. The multi-layered ray acoustics model treats propagation through heterogeneous bone using path-averaged complex wavenumbers and interfacial element-specific transmission and reflection coefficients based on the CT-derived density and acoustic properties of the bone at the surface element [10], [24].

ACKNOWLEDGMENT

The authors would like to thank Dr. Ryan M. Jones for feedback on the manuscript.

REFERENCES

[1] N. Lipsman, M. L. Schwartz, Y. Huang, L. Lee, T. Sankar, M. Chapman, K. Hynynen, and A. M. Lozano, "Mr-guided focused ultrasound thalamotomy for essential tremor: a proof-of-concept study," *The Lancet Neurology*, vol. 12, no. 5, pp. 462–468, 2013.

[2] W. J. Elias, N. Lipsman, W. G. Ondo, P. Ghanouni, Y. G. Kim, W. Lee, M. Schwartz, K. Hynynen, A. M. Lozano, B. B. Shah *et al.*, "A randomized trial of focused ultrasound thalamotomy for essential tremor," *New England Journal of Medicine*, vol. 375, no. 8, pp. 730–739, 2016.

[3] T. Mainprize, N. Lipsman, Y. Huang, Y. Meng, A. Bethune, S. Ironside, C. Heyn, R. Alkins, M. Trudeau, A. Sahgal *et al.*, "Blood-brain barrier opening in primary brain tumors with non-invasive mr-guided focused ultrasound: a clinical safety and feasibility study," *Scientific reports*, vol. 9, no. 1, p. 321, 2019.

[4] Y. Tufail, A. Yoshihiro, S. Pati, M. M. Li, and W. J. Tyler, "Ultrasonic neuromodulation by brain stimulation with transcranial ultrasound," *nature protocols*, vol. 6, no. 9, p. 1453, 2011.

[5] D. Weber-Adrian, E. Thévenot, M. A. O'Reilly *et al.*, "Gene delivery to the spinal cord using mri-guided focused ultrasound," *Gene therapy*, vol. 22, no. 7, pp. 568–577, 2015.

[6] A. H. Payne, G. W. Hawryluk, Y. Anzai, H. Odéen, M. A. Ostlie, E. C. Reichert, A. J. Stump, S. Minoshima, and D. J. Cross, "Magnetic resonance imaging-guided focused ultrasound to increase localized blood-spinal cord barrier permeability," *Neural regeneration research*, vol. 12, no. 12, p. 2045, 2017.

[7] M. A. O'Reilly, T. Chinnery, M.-L. Yee, S.-K. Wu, K. Hynynen, R. S. Kerbel, G. J. Czarnota, K. I. Pritchard, and A. Sahgal, "Preliminary investigation of focused ultrasound-facilitated drug delivery for the treatment of leptomeningeal metastases." *Sci Rep*, vol. 8, p. 9013, 2018.

[8] P. H. F. Nicholson, M. J. Haddaway, and M. W. J. Davie, "The dependence of ultrasonic properties on orientation in human vertebral bone," *Physics in medicine and biology*, vol. 39, no. 6, pp. 1013–1024, 1994.

[9] F. J. Fry and J. E. Barger, "Acoustical properties of the human skull," *The Journal of the Acoustical Society of America*, vol. 63, no. 5, pp. 1576–1590, 1978.

[10] S. Pichardo, V. W. Sin, and K. Hynynen, "Multi-frequency characterization of the speed of sound and attenuation coefficient for longitudinal transmission of freshly excised human skulls," *Physics in medicine and biology*, vol. 56, no. 1, pp. 219–250, 2010.

[11] R. Xu and M. A. O'Reilly, "Simulating transvertebral ultrasound propagation with a multi-layered ray acoustics model," *Physics in medicine and biology*, vol. 63, no. 14, 2018.

[12] G. Clement, J. White, and K. Hynynen, "Investigation of a large-area phased array for focused ultrasound surgery through the skull," *Physics in Medicine & Biology*, vol. 45, no. 4, p. 1071, 2000.

[13] J.-F. Aubry, M. Tanter, M. Pernot, J.-L. Thomas, and M. Fink, "Experimental demonstration of noninvasive transskull adaptive focusing based on prior computed tomography scans," *The Journal of the Acoustical Society of America*, vol. 113, no. 1, pp. 84–93, 2003.

[14] K. Hynynen, G. T. Clement, N. McDannold, N. Vykhodtseva, R. King, P. J. White, S. Vitek, and F. A. Jolesz, "500-element ultrasound phased array system for noninvasive focal surgery of the brain: A preliminary rabbit study with ex vivo human skulls," *Magnetic Resonance in Medicine: An Official Journal of the International Society for Magnetic Resonance in Medicine*, vol. 52, no. 1, pp. 100–107, 2004.

[15] G. F. Pinton, J.-F. Aubry, and M. Tanter, "Direct phase projection and transcranial focusing of ultrasound for brain therapy," *IEEE transactions on ultrasonics, ferroelectrics, and frequency control*, vol. 59, no. 6, pp. 1149–1159, 2012.

[16] L. Deng, M. A. OReilly, R. M. Jones, R. An, and K. Hynynen, "A multi-frequency sparse hemispherical ultrasound phased array for microbubble-mediated transcranial therapy and simultaneous cavitation mapping," *Physics in Medicine & Biology*, vol. 61, no. 24, p. 8476, 2016.

[17] A. Hughes and K. Hynynen, "Design of patient-specific focused ultrasound arrays for non-invasive brain therapy with increased transskull transmission and steering range," *Physics in Medicine & Biology*, vol. 62, no. 17, p. L9, 2017.

[18] G. T. Clement and K. Hynynen, "A non-invasive method for focusing ultrasound through the human skull," *Physics in medicine and biology*, vol. 47, no. 8, p. 1219, 2002.

[19] G. Pinton, J.-F. Aubry, E. Bossy, M. Muller, M. Pernot, and M. Tanter, "Attenuation, scattering, and absorption of ultrasound in the skull bone," *Medical physics*, vol. 39, no. 1, pp. 299–307, 2012.

[20] L. Marsac, D. Chauvet, R. La Greca, A.-L. Boch, K. Chaumoitre, M. Tanter, and J.-F. Aubry, "Ex vivo optimisation of a heterogeneous speed of sound model of the human skull for non-invasive transcranial focused ultrasound at 1 mhz," *International Journal of Hyperthermia*, vol. 33, no. 6, pp. 635–645, 2017.

[21] M. J. Ackerman, "The visible human project," *Proceedings of the IEEE*, vol. 86, no. 3, pp. 504–511, 1998.

[22] L. M. Brekhovskikh and O. A. Godin, "Plane-wave reflection from the boundaries of solids," in *Acoustics of Layered Media I*. Springer, 1990, pp. 87–112.

[23] P. Hasgall, E. Neufeld, M. Gosselin, A. Klingenböck, and N. Kuster, "Itis database for thermal and electromagnetic parameters of biological tissues," *Version 3.1*, 2015.

[24] S. Pichardo, C. Moreno-Hernández, R. A. Drainville, V. Sin, L. Curiel, and K. Hynynen, "A viscoelastic model for the prediction of transcranial ultrasound propagation: application for the estimation of shear acoustic properties in the human skull," *Phys. Med. Biol*, vol. 62, pp. 6938–6962, 2017.

[25] Y. Y. Botros, E. S. Ebbini, and J. L. Volakis, "Two-step hybrid virtual array ray(var) technique for focusing through the rib cage," *IEEE transactions on ultrasonics, ferroelectrics, and frequency control*, vol. 45, no. 4, pp. 989–1000, 1998.

[26] S. Bobkova, L. Gavrilov, V. Khokhlova, A. Shaw, and J. Hand, "Focusing of high-intensity ultrasound through the rib cage using a therapeutic random phased array," *Ultrasound in medicine & biology*, vol. 36, no. 6, pp. 888–906, 2010.

[27] E. Cochard, C. Prada, J.-F. Aubry, and M. Fink, "Ultrasonic focusing through the ribs using the dort method," *Medical physics*, vol. 36, no. 8, pp. 3495–3503, 2009.

[28] P. Gélat, G. Ter Haar, and N. Saffari, "Modelling of the acoustic field of a multi-element hifu array scattered by human ribs," *Physics in Medicine & Biology*, vol. 56, no. 17, p. 5553, 2011.

[29] ——, "The optimization of acoustic fields for ablative therapies of tumours in the upper abdomen," *Physics in Medicine & Biology*, vol. 57, no. 24, p. 8471, 2012.

[30] ——, "A comparison of methods for focusing the field of a hifu array transducer through human ribs," *Physics in Medicine & Biology*, vol. 59, no. 12, p. 3139, 2014.

[31] J. Robin, A. Simon, B. Arnal, M. Tanter, and M. Pernot, "Self-adaptive ultrasonic beam amplifiers: application to transcostal shock wave therapy," *Physics in Medicine & Biology*, vol. 63, no. 17, p. 175014, 2018.

[32] Y.-S. Kim, M. J. Park, H. Rhim, M. W. Lee, and H. K. Lim, "Sonographic analysis of the intercostal spaces for the application of high-intensity focused ultrasound therapy to the liver," *American Journal of Roentgenology*, vol. 203, no. 1, pp. 201–208, 2014.

[33] M. Hajibozorgi and N. Arjmand, "Sagittal range of motion of the thoracic spine using inertial tracking device and effect of measurement errors on model predictions," *Journal of biomechanics*, vol. 49, no. 6, pp. 913–918, 2016.

[34] S.-M. P. Fletcher and M. A. O'Reilly, "Analysis of multi-frequency and phase keying strategies for focusing ultrasound to the human vertebral canal," *IEEE transactions on ultrasonics, ferroelectrics, and frequency control*, 2018.

[35] N. McDannold, N. Vykhodtseva, and K. Hynynen, "Blood-brain barrier disruption induced by focused ultrasound and circulating preformed microbubbles appears to be characterized by the mechanical index," *Ultrasound in medicine & biology*, vol. 34, no. 5, pp. 834–840, 2008.

[36] T. Grau, R. Leipold, S. Delorme, E. Martin, and J. Motsch, "Ultrasound imaging of the thoracic epidural space," *Regional anesthesia and pain medicine*, vol. 27, no. 2, pp. 200–206, 2002.

[37] R. M. Jones, L. Deng, K. Leung, D. McMahon, M. A. O'Reilly, and K. Hynynen, "Three-dimensional transcranial microbubble imaging for guiding volumetric ultrasound-mediated blood-brain barrier opening," *Theranostics*, vol. 8, no. 11, p. 2909, 2018.

[38] H. O'Neil, "Theory of focusing radiators," *The Journal of the Acoustical Society of America*, vol. 21, no. 5, pp. 516–526, 1949.

[39] X. Fan and K. Hynynen, "The effects of curved tissue layers on the power deposition patterns of therapeutic ultrasound beams," *Medical physics*, vol. 21, no. 1, pp. 25–34, 1994.

[40] R. M. Jones and K. Hynynen, "Comparison of analytical and numerical approaches for ct-based aberration correction in transcranial passive acoustic imaging," *Physics in Medicine & Biology*, vol. 61, no. 1, p. 23, 2016.

[41] W. Limthongkul, E. E. Karaikovic, J. W. Savage, and A. Markovic, "Volumetric analysis of thoracic and lumbar vertebral bodies," *The Spine Journal*, vol. 10, no. 2, pp. 153–158, 2010.

[42] I. Busscher, J. J. Ploegmakers, G. J. Verkerke, and A. G. Veldhuizen, "Comparative anatomical dimensions of the complete human and porcine spine," *European Spine Journal*, vol. 19, no. 7, pp. 1104–1114, 2010.

[43] P. A. Yushkevich, J. Piven, H. C. Hazlett, R. G. Smith, S. Ho, J. C. Gee, and G. Gerig, "User-guided 3d active contour segmentation of anatomical structures: significantly improved efficiency and reliability," *Neuroimage*, vol. 31, no. 3, pp. 1116–1128, 2006.

[44] Q. Fang and D. A. Boas, "Tetrahedral mesh generation from volumetric binary and grayscale images," in *Biomedical Imaging: From Nano to Macro, 2009. ISBI'09. IEEE International Symposium on*. Ieee, 2009, pp. 1142–1145.

[45] J. White, G. T. Clement, and K. Hynynen, "Transcranial ultrasound focus reconstruction with phase and amplitude correction," *ieee transactions on ultrasonics, ferroelectrics, and frequency control*, vol. 52, no. 9, pp. 1518–1522, 2005.

[46] J. Sutton, Y. Power, Y. Zhang, N. Vykhodtseva, and N. McDannold, "Design, characterization, and performance of a dual aperture, focused ultrasound system for microbubble-mediated, non-thermal ablation in rat brain," *The Journal of the Acoustical Society of America*, vol. 138, no. 3, pp. 1821–1821, 2015.

[47] T. Sun, J. T. Sutton, C. Power, Y. Zhang, E. L. Miller, and N. J. McDannold, "Transcranial cavitation-mediated ultrasound therapy at sub-mhz frequency via temporal interference modulation," *Applied Physics Letters*, vol. 111, no. 16, p. 163701, 2017.

[48] B. E. Treeby and B. T. Cox, "k-wave: Matlab toolbox for the simulation and reconstruction of photoacoustic wave fields," *Journal of biomedical optics*, vol. 15, no. 2, p. 021314, 2010.

[49] R. M. Jones, M. A. O'Reilly, and K. Hynynen, "Experimental demonstration of passive acoustic imaging in the human skull cavity using ct-based aberration corrections," *Medical physics*, vol. 42, no. 7, pp. 4385–4400, 2015.

[50] X. Fan and K. Hynynen, "The effect of wave reflection and refraction at soft tissue interfaces during ultrasound hyperthermia treatments," *The Journal of the Acoustical Society of America*, vol. 91, no. 3, pp. 1727–1736, 1992.

[51] N. Ellens and K. Hynynen, "Simulation study of the effects of near-and far-field heating during focused ultrasound uterine fibroid ablation using an electronically focused phased array: A theoretical analysis of patient safety," *Medical physics*, vol. 41, no. 7, 2014.

[52] L. Fradet, P.-J. Arnoux, J.-P. Ranjeva, Y. Petit, and V. Callot, "Morphometrics of the entire human spinal cord and spinal canal measured from in vivo high-resolution anatomical magnetic resonance imaging," *Spine*, vol. 39, no. 4, pp. E262–E269, 2014.

[53] Y. Y. Botros, J. L. Volakis, P. VanBaren, and E. S. Ebbini, "A hybrid computational model for ultrasound phased-array heating in presence of strongly scattering obstacles," *IEEE Transactions on Biomedical Engineering*, vol. 44, no. 11, pp. 1039–1050, 1997.

[54] B. E. Treeby, J. Jaros, A. P. Rendell, and B. Cox, "Modeling nonlinear ultrasound propagation in heterogeneous media with power law absorption using a k-space pseudospectral method," *The Journal of the Acoustical Society of America*, vol. 131, no. 6, pp. 4324–4336, 2012.

[55] N. P. Ellens, B. B. Lucht, S. T. Gunaseelan, J. M. Hudson, and K. H. Hynynen, "A novel, flat, electronically-steered phased array transducer for tissue ablation: preliminary results," *Physics in Medicine & Biology*, vol. 60, no. 6, p. 2195, 2015.

[56] S. Pichardo and K. Hynynen, "Treatment of near-skull brain tissue with a focused device using shear-mode conversion: a numerical study," *Physics in medicine and biology*, vol. 52, no. 24, p. 7313, 2007.